Strained Surface Structure in the Growth of Quantum Dots

The formation of Ge self-organized quantum dots (huts) on the Si(001)-2x1 surface has attracted much attention due to its status as the premier model system for investigating strain-induced semiconductor nanostructure growth. Our findings on this strained surface structure imply that both the structure and the strain of semiconductor nanostructures may be controlled through the understanding of their surface properties.

Although the hut structures are known to have a highly ordered structure defined by four Ge{105} facets, little was known about the structure until our investigation. We found using field ion scanning tunneling microscopy (FI-STM) that the Ge(105)-1x2 surface structure exhibits significant bias dependent on its filled or empty states. (Fig. 1(B), Fujikawa *et al*., Phys. Rev. Lett. **88**, 176101 (2002).) With the help of first-principle calculations, we proposed a new model consisting of rebonded steps (RS model). Additionally, direct observations of the RS structure were achieved by a high-performance non-contact atomic force microscope (AFM), resolving all individual dangling bonds (Fig. 1(A)) [1]. This surface structure is characterized by strong surface strain coming from the rebonded structure unit, which was found to relax by lattice mismatch strain applied from the Si substrate. Distorted bonding configuration of the surface atoms, which resulted from strong charge transfer, is found to also be responsible for surface strain relaxation. This charge transfer was documented at an atomic level by Kelvin-force microscopy (KFM) [1] and scanning tunneling spectroscopy (STS) [2]. We successfully obtained an atomically-resolved quantitative surface potential map by KFM for the first time, which agrees well with the theoretical calculations of the surface electronic states. The STS results indicate that the surface charge transfer is explained by the uneven distribution of surface bands, rather than the separated electron filling of localized dangling bonds.
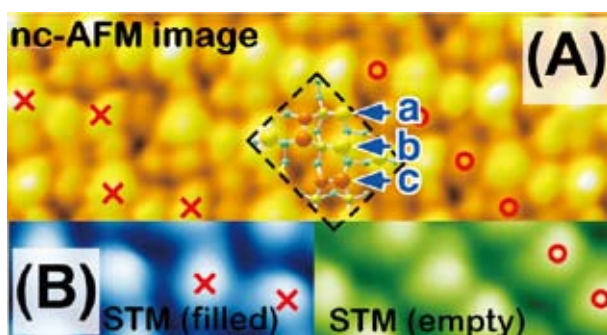
The RS model reveals the importance of tensile surface

Fig. 1. (A) Non-contact AFM and (B) STM images of the Ge(105)-1x2 surface. The surface unit cell of Ge{105}-1x2 reconstruction with a size of 10.86 Å x 13.84 Å is described as a broken rectangle, and the surface atomic structure of the RS model is superimposed on the AFM image. The dangling bonds on atoms a, b and dimer c are clearly resolved as separate protrusions in our AFM observation. The filled- and empty-state STM images exhibit distinctive differences, which are well understood by the calculated density of states based on our RS structure model accompanied with charge transfer from dimer c (marked by circles) to atoms a and b (marked by crosses).

strain on the rebonded steps. For example, hydrogen adsorption dramatically destabilizes the Ge/Si(105) surface, which can be understood by the fact that hydrogen adsorption increases the surface strain by causing rebonded surface dimers to be placed at asymmetric positions (Fig. 2) [3]. Our STM observations reveal that hydrogen adsorption causes defect formations on the SiGe(105) surface formed on the Si(105) substrates, which proves the strain enhancement effect described above. This result explains the previously observed phenomenon of hydrogen suppressing Ge hut formation on Si(001) (surfactant effect).
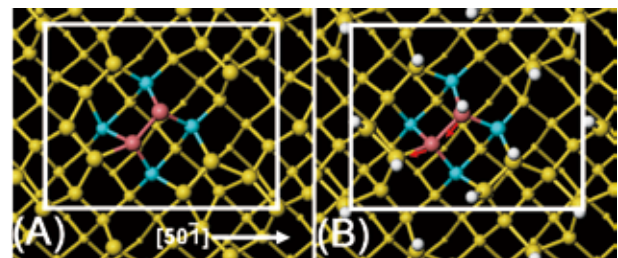

Fig. 2. Simulated atomic structures of (A) clean and (B) hydrogen-terminated Ge/Si(105) surfaces. The solid rectangles show 1x2 unit cells of the surface structure. Hydrogen atoms (white) change the bonding configuration of the surface atoms by causing the rebonded dimers (red) to be placed on the surrounding Ge atoms (blue) in a stressed manner.

Our recent observations of Si island growth on Ge(001) reveal that all of the {105}-related features observed in Ge/Si island formation completely disappear in the oppositely strained Si/Ge islands, while some similarity remains between them reflecting the symmetric response of the bulk strain. This fact indicates that the tensily-strained {105} facet structure plays a critical role in structure determination of the strained island, reacting asymmetrically to the lattice mismatch strain from the substrate.

The strained facet structure on quantum dots, established by our detailed atomic-scale characterizations using scanning probe techniques, was found to play an important role in their structure determination through its unique response to lattice mismatch strain as well as surface conditions such as adsorption. This unique response would make the structure as well as the strain of the quantum dots controllable.

References
[1] T. Eguchi, Y. Fujikawa, K. Akiyama, T. An, M. Ono, T. Hashimoto, Y. Morikawa, K. Terakura, T. Sakurai, M. G. Lagally, and Y. Hasegawa, Phys. Rev. Lett. **93**, 266102 (2004).
[2] Y. Fujikawa, T. Sakurai and M. G. Lagally, Appl. Surf. Sci. **252**, 5244-5248 (2006).
[3] Y. Fujikawa, T. Nagao, Y. Yamada-Takamura, T. Sakurai, T. Hashimoto, Y. Morikawa, K. Terakura and M. G. Lagally, Phys. Rev. Lett. **94**, 086105 (2005).

Contact to
Yasunori Fujikawa (Surface and Interface Research Division)
e-mail: fujika-0@imr.tohoku.ac.jp

Superelasticity in Ti–10V–2Fe–3Al Alloys with Nitrogen Addition

Recently, much attention has been paid to Ni-free β titanium shape memory/superelastic alloys for biomedical use. For wider application, however, reduction of production cost is important. Interstitial elements, which were not used previously due to the deterioration of ductility/toughness, exhibit large solution strengthening and were recently applied in industrial development of low-cost titanium alloys. We reported new superelastic alloys by addition of nitrogen to Ti-10V-2Fe-3Al which is originally used for airplanes [1,2].

Fig.1 schematically describes the concept of alloy development. Nitrogen suppresses plastic deformation of β by increasing the yield strength of β (σ^{β}_{y}). Further, it suppresses β→ω and β→α" martensitic transformations (see the change of transformation starting temperatures, ω_s and M_s). As a result, the stress-induced β→α" martensitic transformation occur in a wider temperature range, and the potential of superelasticity is increased (highlighted in purple). In-situ observation of surface relieves during tensile deformation (Figs. 2(a)-(c)) shows clearly that stress-induced α" martensite is formed by deformation and reversely transformed to β matrix by unloading in the alloy containing 0.2mass%N. This is a direct evidence of the occurrence of superelasticity. Fig. 2(d) shows the recovered strain obtained in cyclic tensile tests. Total elastic strain reaches to 2% with the addition of nitrogen by increasing pure elastic strain through strengthening and enhancement of superelasticity.

References
[1] T. Furuhara, S. Annaka and T. Maki, J. Mater. Eng. Perform. **14**, 761 (2005).
[2] T. Furuhara, S. Annaka, Y. Tomio and T. Maki, Mater. Sci. Engng. A, **438-440**, 825 (2006).

Contact to
Tadashi Furuhara (High Purity Metallic Materials Division)
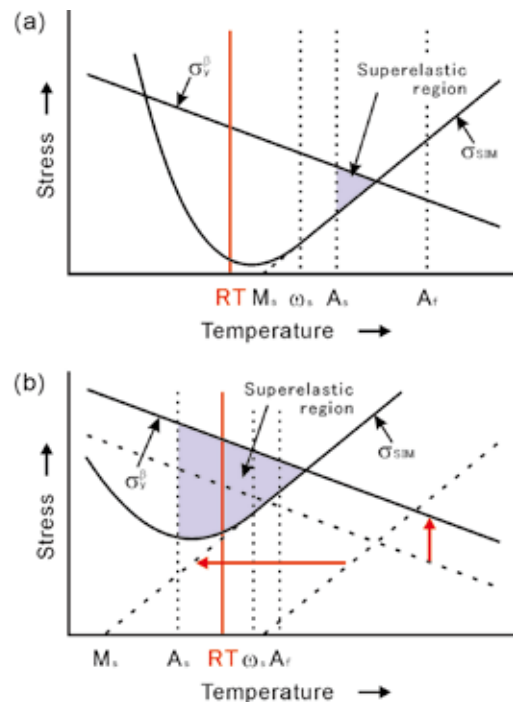e-mail: furuhara@imr.tohoku.ac.jp

Fig. 1: Improvement of superelasticity with nitrogen addition. (a) nitrogen free alloy, (b) nitrogen-added alloy; σ_{SIM} : stress required to induce the martensitic transformation. A_s and A_f : temperatures where the reverse transformation starts and ends, respectively.
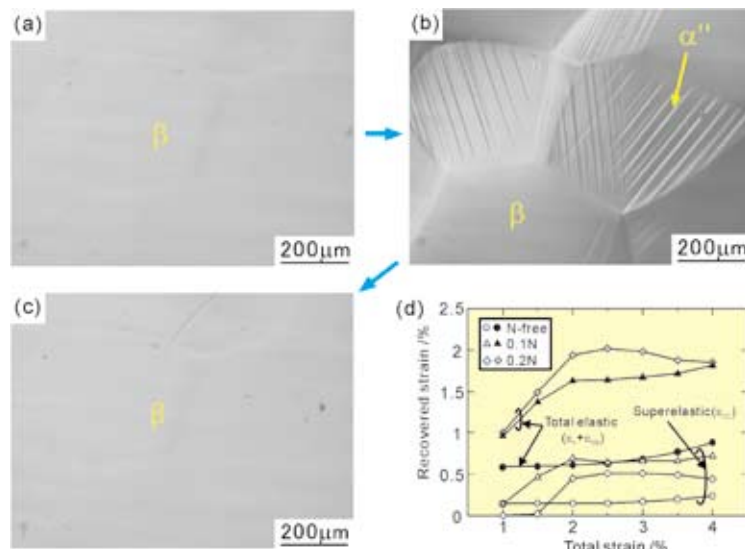

Fig. 2: (a)-(c) Optical micrographs showing the formation and reversion of surface relieves during 1.5% tensile deformation and unloading at room temperature in the Ti-10V-2Fe-3Al-0.2N alloy, respectively.; (d) variation of total elastic and superelastic strains recovered with total applied strain in cyclic tensile tests.

Effects of Morphology and Doping on the Electronic and Structural Properties of Hydrogenated Silicon Nanowires

Using first principles based calculations, we explore the different avenues of applications of Si-nanowires. We show the novel reconstructions on the surfaces of the nanowires, interpretation of STM images, sensors capabilities of bio- and chemical species and designed p-, n-doped and optical nanowires. This study has been one of the major contributions to the area of Si-nanowires and their applications.

Si-nanowires (SiNWs) are considered as the strongest candidates for nanoelectronics due to their electrical and optical properties, controlled production [1], and promising new applications such as molecular scale sensors. These applications rely heavily on the electronic structure of SiNWs and require precise control of the surface atomic and electronic structures. For the rapid development of this field, advances in the understanding of the electronic structure of SiNWs and the various possible ways to modify it, are very important [2, 3].
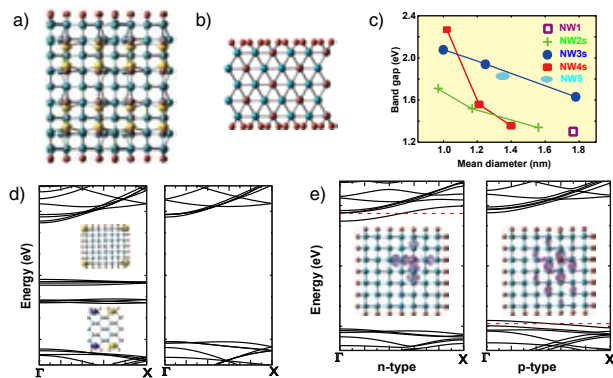

Fig 1. a) Novel reconstructions on the surfaces b) correct interpretation of STM c) tailor made optical properties d) circuit elements e) nanosensors.

In order to address these issues, we have studied geometries of five different classes of SiNWs (referred as NWn (n=1-5)) differing in orientations and surface morphologies Fig. 2. The band gap changes with the orientation and thickness of the nanowires. Importantly, it also depends strongly upon the surface morphologies.
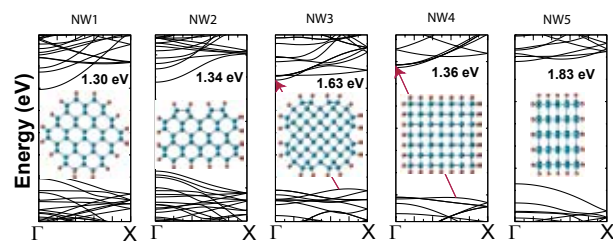

Fig. 2 The band structures of SiNWs: NW1, NW2, NW3, NW4, and NW5. Insets: shows their corresponding atomic structure.

In order to determine the surface sensitivity of SiNWs, we study the effects of changing the concentration of H on the surface of NW4 nanowires as they involve only (110) facets. Removal of one H atom from each of the corner Si atoms of the NW4 nanowire has an effect of creating unpaired electrons on the surface, which leads to drastic changes in the band structure. In contrast to this, we find that SiNWs with (100) facets can easily offset the effects of H deficit on the surface by dimerization such as in NW2 and NW3. This shows that the electronic properties of nanowires with (100) surfaces cannot be easily modified and therefore are poor candidate for the sensors. Nanowires with (110) or (111) surfaces are ideal for sensors as their electronic properties could be modified drastically by changing H concentration.

Due to significant differences in the electronic properties of NW1 and NW4 by a change in hydrogen concentration, we considered them as our prototypes and doped them with B and P to have p- and n-type nanowires, respectively. The band structures of the doped nanowires show a shift of the Fermi level towards the valence and conduction band for the p- and n- type SiNW, respectively. Nanowires grown along different directions and with different surface morphologies have different dispersions (Fig. 2) in their conduction and valence bands and this information can be used to design doped semiconductors with better conduction properties.

In summary, we show these nanowires could be ideal for applications such as optoelectronic devices, and lasers. Further we have shown for the first time that H-defects on nanowires with (110) facets modify their electronic properties significantly so that they could be used as sensors and that the behavior of n- or p- type doping in hydrogenated SiNWs is very similar to bulk or oxidized thicker nanowires, therefore establishing them to be the smallest possible building blocks for silicon based nanoscale devices [2, 3].

References

[1] A. M. Morales and C. M. Lieber, Science **279**, 208 (1998).
[2] A. K. Singh, V. Kumar, R. Note and Y. Kawazoe, Nano Lett. **5**, 2302 (2005).
[3] A. K. Singh, V. Kumar, R. Note and Y. Kawazoe, Nano Lett. **6**, 920 (2006).

Contact to
Yoshiyuki Kawazoe (Materials Design by Computer simulation Division)
e-mail: kawazoe@imr.edu

X-ray Standing Wave and Atomic Resolution Holography using X-ray Excited Optical Luminescence

X-ray excited optical luminescence (XEOL) was applied to the x-ray standing wave (XSW) method and atom-resolved x-ray holography (XH). We measured the incident beam angular dependence of the luminescence intensity from a ZnO-coated Al₂O₃, and found that it corresponded to the XSW/XH pattern of an Al₂O₃. The present result demonstrates that hard x-ray XSW/XH studies for light elements, which have been difficult by fluorescence detection, can easily be carried out by XEOL detection.

When x rays are irradiated on solids, scattering x rays, fluorescent x rays, photoelectrons and Auger electrons are typically emitted. In addition, some materials emit visible, infrared or ultraviolet rays; this phenomenon is called x-ray excited optical luminescence (XEOL). XEOL has been applied to site-selective XAFS measurements, whereas XAFS techniques using x-ray fluorescence and transmittance cannot be used for such measurements. On the other hand, the x-ray standing wave (XSW) method and atomic-resolution x-ray holography (XH)[1,2], which together enable us to determine the local structure around a specified atom, normally use x-ray fluorescence from the specified atom, but there has been no report on the use of XEOL to date.

Thus, we measured the XEOL intensity variation of a ZnO-coated sapphire single crystal with a change in the incident beam direction, and we discuss the possibility of XSW/XH measurements. The XSW/XH experiment was conducted at undulator beamline BL37XU in the SPring-8 synchrotron radiation facility. Figure 1 (a) shows angular anisotropies of the XEOL intensity. The pattern in Fig. 1 (a) exhibits clear XSW lines, implying that XSW/XH data were recorded by the XEOL detection. To estimate the validity of this calculation more exactly, the $30\bar{3}0$ lines in Fig. 1 (a) were

averaged over the k_y-direction, as shown in Fig. 1(b). The position and amplitude of the experimental pattern well agree with those of the calculated pattern.

Next, we applied the scattering pattern extraction algorithm using the maximum-entropy method (SPEA-MEM) to the pattern in Fig. 1(a) to reconstruct the atomic images. Figure 2 shows the obtained real space image for the (0001) plane at z =1.1 Å, in which O atoms exist. Circles in Figs. 2 indicate theoretical positions of O atoms. Al occupies two distinct sites in the (0001) plane, and therefore, two types of environments are overlapped in Fig. 2. Oxygen atoms seem to be reconstructed despite the smallness of their scattering cross sections. The XSW/XH measurement using x-ray fluorescence is generally difficult for light elements, such as Al or Si, because of their small cross sections for inner-shell ionization and the absorption of their fluorescence by air. Our results demonstrate that hard x-ray XSW/XH measurement is possible for light elements using XEOL.[3,4]

References

[1] K. Hayashi, Advances in Imaging and Electron Physics **140**, 119 (2006) .

[2] S. Hosokawa, T. Ozaki, K. Hayashi, N. Happo, M. Fujiwara, K. Horii, P. Fons, A. V. Kolobov, J. Tominaga, Appl. Phys. Lett. **90**, 1361913 (2007).

[3] K. Hayashi, T. Hayashi, T. Shishido, E. Matsubara, H. Makino and T. Yao, Bunseki Kagaku **55**, 441 (2006). (Japanese).

[4] K. Hayashi, T. Hayashi, T. Shishido, E. Matsubara, H. Makino, T. Yao and T. Matsushita, Phys. Rev. B 76, 014119 (2007).

Contact to
Kouichi Hayashi (Chemical Physics of Non-Crystalline Materials Division)
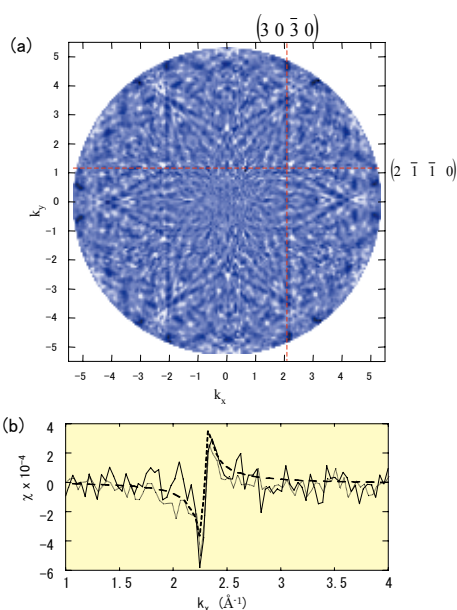e-mail: khayashi@imr.tohoku.ac.jp

Fig. 1 XSW/XH patterns produced by luminescence from ZnO/Al₂O₃. (a) Pattern on k_x-k_y plane. (b) XSW line profile averaged over k_y-direction
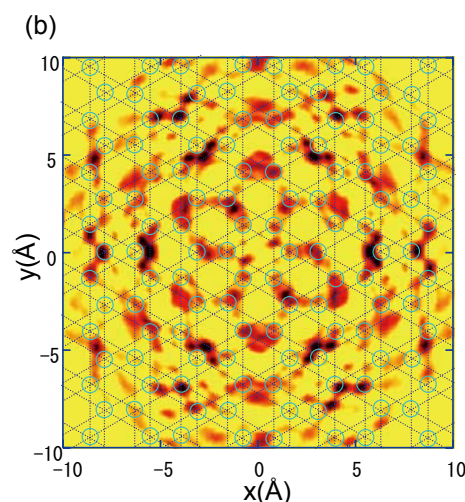

Fig. 2 Real-space images reconstructed from hologram in Fig. 1 (a) by SCEA-MEM. The plane is parallel to the {001} lattice plane, and is 1.1 Å above the Al atom. Circles indicate theoretical O positions.

Creation of Multi-functional Titanium Alloys with Low Elastic Moduli for Biomedical Applications

Ti-Nb-Ta-Zr system alloy exhibits the functionalities such as low Young's modulus, super elasticity, and shape memory effect. The Ti-Nb-Ta-Zr system alloy is expected to be highly competitive biomedical β-type titanium alloy in the world.

Titanium alloys have been receiving much attention as high biocompatible material with a modulus similar to that of bone. Thus, a number of titanium alloys have been currently developed for biomedical applications. Especially, the β-type Ti-29Nb-13Ta-4.6Zr alloy, which has been designed by DV-Xα cluster method targeting a low Young's modulus and high workability by Niinomi et al., is a titanium alloy composed of non-toxic and allergy-free elements for biomedical applications [1]. It has been reported that this alloy possesses excellent properties that are required for biomaterials. Recently, it has been reported that there is a high possibility for Ti-Nb-Ta-Zr system alloy to exhibit super elasticity because the behavior of stress-strain curve at tensile loading is nearly equal to that of super elastic alloys such as TiNi alloy, which has been already put into practical applications. However, the numbers of the reports on the effects of alloying elements on the various properties of the Ti-Nb-Ta-Zr system alloys including the Ti-29Nb-13Ta-4.6Zr alloy are few. Therefore, the effects of conditions of fabrication and thermo-mechanical treatments, and alloying elements on the mechanical properties, tensile deformation behaviors and biocompatibility of the Ti-Nb-Ta-Zr system alloys were investigated with relating to nano/micro-structures in this study.

The cell viability of Ti-Nb-Ta-Zr system alloy, where the hot forged Ti-29Nb-13Ta-4.6Zr was applied, was nearly the same as that of pure Ti, which has relatively good biocompatibility, and greater than that of Ti-6Al-4V ELI, which is a representative α+β titanium alloy, in both as-extracted and filtrated extracted solutions. Namely, it was confirmed that the nontoxicity of Ti-29Nb-13Ta-4.6Zr is equivalent to that of pure Ti and is greater than that of Ti-6Al-4V.

Young's moduli of the Ti-XNb-10Ta-5Zr alloys subjected to swaging after fabrication using power metallurgy method decrease with an increase in the Nb content as shown in Fig 1. However, the Young's moduli of the Ti-XNb-10Ta-5Zr alloys with 15 mass%, 20 mass%, and 25 mass% Nb, which have ω phase, exhibit a reverse trend. The Ti-25Nb-10Ta-5Zr alloy exhibits the greatest elongation among the other Ti-XNb-10Ta-5Zr alloys because multi-deformation mechanisms act simultaneously. Stress-induced transformation of metastable β phase to martensite phase, and its reversion are recognized in the Ti-XNb-10Ta-5Zr alloys with 20 mass% and 25 mass% Nb at tensile loading-unloading as shown in Fig. 2. The shape memory effect and the super elastic property are expected to be achieved in these types of the Ti-Nb-Ta-Zr system alloys. The elastic deformation behavior of the Ti-30Nb-10Ta-5Zr alloy disobeys Hooke's law. In this case, the maximum elastic strain is around 2.9%.

The wires of the Ti-29Nb-13Ta-4.6Zr alloy with diameters of 0.3 and 1.0 mm fabricated by thermo-mechanical
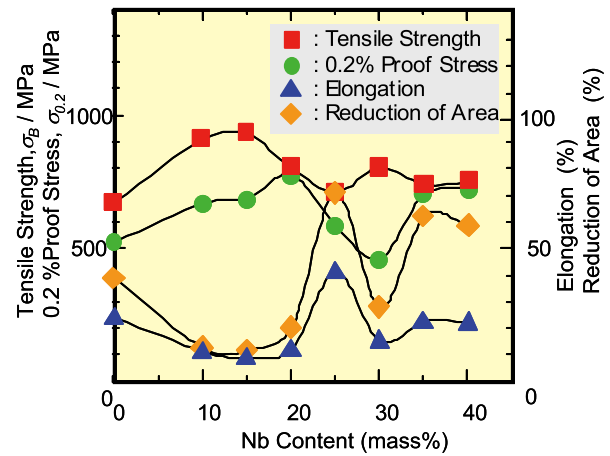

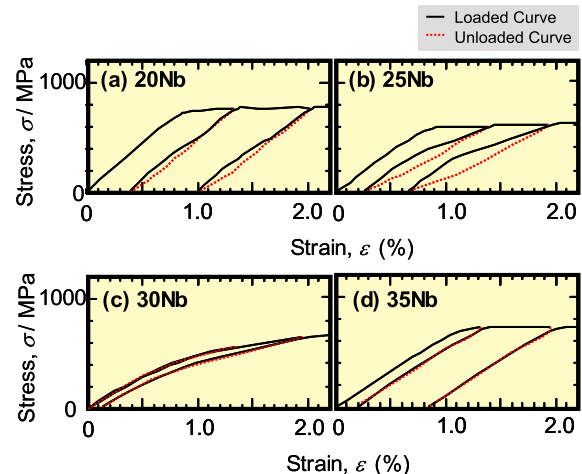Fig. 1 Mechanical properties of Ti-XNb-10Ta-5Zr alloy as a function of Nb content.

Fig. 2 Tensile loading - unloading stress-strain curves of Ti-X(= (a) 20Nb, (b) 25Nb, (c) 30Nb, and (d) 35Nb)Nb-10Ta-5Zr alloys.

processing including cold-drawing and heat treatment also show an unique elastic behavior with two gradients under tensile loading. Their maximum elastic strains are around 2.8 and 2.9%, respectively, which are around twice higher than that of the hot forged Ti-29Nb-13Ta-4.6Zr alloy subjected to a solution treatment. Therefore, it is highly expected to be applied to dental and surgical wires.

From these results, in this study, an important guideline can be obtained for designing new titanium alloys for medical applications, which have the functionalities such as low Young's modulus, shape memory effect and super elasticity.

Reference
[1] M. Niinomi, Int. J. Fatigue, **29**, 992 (2007).

Contact to
Mitsuo Niinomi (Biomaterials Science Division)
e-mail: niinomi@imr.tohoku.ac.jp

Nano / Micro Structure Controlled Materials

Fabrication and Applications of Bulk Metallic Glasses

This article reviews our results of the formation and resultant applications of bulk metallic glasses (BMGs). The BMGs have become to be fabricated considerably stably since the early 1990's owing to endeavors of Dr. Inoue who has played a leading role in fusing academia and industry to create superior materials.

Dr. Akihisa Inoue and his colleagues have discovered a novel phenomenon that disproved this common theory. Dr. Inoue et al. found that if a metallic liquid is gently cooled below its melting point at a slow rate such as approximately 10 K/s, a supercooled metallic liquid can maintain its state without crystallization and produces a stable glassy bulk metal (Fig. 1). Dr. Inoue and coworkers have examined the factors involved in this novel phenomenon and have determined the generation mechanism using experiments and computational algorithms. His work has advanced both basic and applied materials science technologies. In other words, his group has elucidated that a glassy bulk metal is stably fabricated in an alloy system if the following three empirical rules (i.e., three components rule) are satisfied [1]. 1) The system must be comprised of multi-components where each component is ternary or greater. 2) The atomic radius of each component must differ by at least approximately 12%. 3) A negative heat must be produced when mixing the elements. Furthermore, Inoue's group has experimentally demonstrated that these alloy solid systems are structured into dense random packing states that have short-range order atomic configurations compared to conventional amorphous materials. They have also revealed that even though a metal-metal alloy system is in an icosahedral cluster state, a metal-quasimetal alloy system is formed with new local atomic configurations based on a transformed trigonal prism network, which confers the stability of these new alloy systems.

In addition, Inoue and coworkers have demonstrated that an algorithm based on the three empirical rules accurately predicts the composition range for forming metallic glasses and the degree of composition dependency on the stability of the supercooled liquids. These findings led Inoue to propose a theory for developing new materials.

His theory has led to the discovery of several hundreds of glassy bulk metal alloy systems of Mg, rare earth metals (lanthanide), Zr, Ti, Hf, Fe, Pd, Co, No, Cu, Ca, and Pt. Inoue et al. have also successfully fabricated rod-like materials with maximum diameters of 80 mm or more, which has enabled upsized materials to finally be produced. The measured quenching rates were extremely low and the slowest rate recorded was 0.02 K/s. In contrast, manufacturing conventional amorphous alloy systems requires an ultra rapid quenching (10^6 K/s), which is difficult to control and limits the widths to several tens of micrometers.

Non-equilibrium materials such as bulk metal glasses have been rapidly industrialized and have already been applied to various products. These products include electromagnetic and shielding materials, materials for machines, robots, bicycles, wheel-chairs, electrodes, optic mirrors and junction terminals, anti-abrasion materials, materials for shot-peening balls, glasses and cell-phone frames, moldings, accessories, tools, fishing rods, golf clubs, tennis rackets, and baseball bats.

Furthermore, the development and commercialization of bulk metal glass materials have been actively explored for use in automobile pressure sensors, the world smallest 2.4 mm-diameter high tork gear motor (Fig. 2), sensor pipes for Coriori flowmeters, York materials for linear actuators, biomaterials, materials for medical devices, portable electronic devices, spring materials, materials for high-speed transporting equipment, materials for fuel cells, impact absorbents, etc. The frontier spirit and endless creativity of the Inoue group has significantly contributed to the development of "supercooled metal science" [3-4].
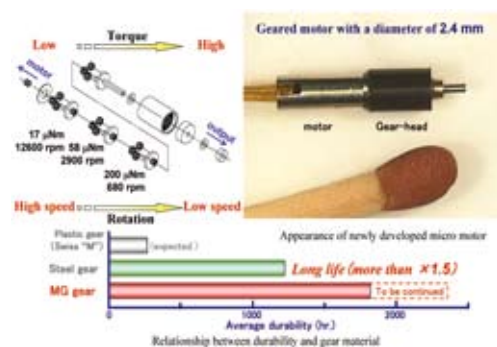
Fig. 2 Outlook and durability of a micro-geared motor of 2.4 mm in diameter constructed by using two super precision sun-carrier gears made of Ni-based glassy alloy [2].

References

[1] A. Inoue, Acta Mater. **48**, 279 (2000).

[2] A. Inoue, B.L. Shen and A. Takeuchi, Mater. Sci. Eng., **A 441**, 18 (2006).

[3] A. Inoue, Proc. Jpn. Acad. Ser. B-Phys. Biol. Sci., **81**, 156 (2005).

[4] A. Inoue, Proc. Jpn. Acad. Ser. B-Phys. Biol. Sci., **81**, 172 (2005).

Contact to
Akira Takeuchi (Non-Equilibrium Materials Division)
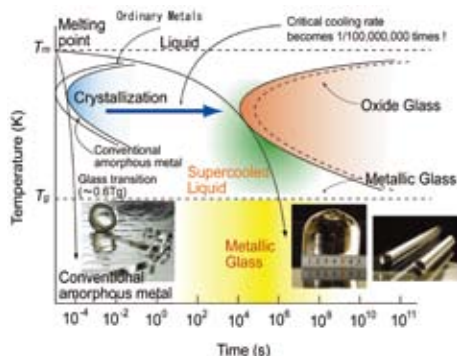e-mail: nano2000@imr.tohoku.ac.jp

Fig. 1 Schematic illustration showing fabrications of tape-shaped conventional amorphous alloy (thickness: ~ 20 μm) and bulk metallic glasses (BMGs) (~ maximum diameter: 72 mm), both from a liquid phase. Followed by a couple of decades of the regime of "amorphous alloy" since its first success in 1960, now, one can steadily fabricate BMGs owing to findings by Dr. Inoue. Furthermore, researches on applications and developments utilizing BMGs as engineering materials have also opened up through the success in fabricating BMGs.

Preparation of TiC-TiB₂-SiC Ternary Eutectic Composite

TiC-TiB₂-SiC composites were synthesized by arc and floating zone (FZ) melting using TiC, TiB₂ and β-SiC powders as starting materials. In TiC-TiB₂-SiC system, a ternary eutectic composition of 34TiC-22TiB₂-44SiC (mol%) and three binary eutectic compositions of 40TiB₂-60SiC, 28TiB₂-72TiC and 40TiC-60SiC (mol%) were found. TiC(022), TiB₂(010) and SiC(111) in the eutectic composite were perpendicular to the growth direction. The TiC-TiB₂-SiC ternary eutectic composite had the relationship among crystal planes: TiC[011]//TiB₂[010]//SiC[112], TiC(200)// TiB₂(001)//SiC(40$\overline{2}$) and TiC(111)//TiB₂(10$\overline{1}$)//SiC($\overline{2}$20).

TiC-TiB₂-SiC system composites can be an excellent material due to several combined properties of TiC, TiB₂ and SiC, such as excellent oxidation resistance, high hardness and high electrical conductivity. The composites of carbide and boride have been prepared by conventional solid state sintering methods. On the other hand, the self-assembly of microstructure during the solidification of melted ceramic materials is a useful technique to develop high-performance composite materials. Particularly, an eutectic texture may improve the properties of ceramic composites. Some promising results have been reported for the B₄C-SiC, B₄C-TiB₂ and B₄C-TiB₂-SiC eutectic composites by our research group. However, the study on the TiC-TiB₂-SiC eutectic composite has not been reported.

TiC, TiB₂ and SiC powders were weighed and mixed, and then pressed into disks with 10 mm in diameter. The specimens were melted and solidified on a water-cooled copper holder by arc-melting. The mixture powders were also isostatically pressed in a latex tube with 10 mm in diameter. The pressed rods were sintered at 1873 K for 3.6 ks and then directionally melted by FZ using a Xe lamp heater in an Ar atmosphere.

Figure 1 demonstrates the phase diagram of TiC-TiB₂-SiC ternary system and the microstructure of binary and ternary eutectic composites [1]. The binary eutectic points were abbreviated as BE1 for 40TiB₂-60SiC, BE2 for 28TiB₂-72TiC [2] and BE3 for 40TiC-60SiC (mol%). The TiC-TiB₂-SiC ternary eutectic composition was determined as 34TiC-22TiB₂-44SiC (mol%) and abbreviated as TE. The microstructure can be categorized into TiB₂+TE, TiC+TE, TE+BE1, SiC+BE1, TiB₂+BE1, TiC+SiC+TE and TiB₂+TiC+TE. BE1 and BE2 showed labyrinthine microstructures, whereas BE3 and TE showed typical lamellar textures. TiC, TiB₂ and SiC grains in the ternary eutectic composite showed a lamellar texture of 3, 3 and 2 µm in thickness, respectively, and paralleled to each other along the growth direction (Fig. 1 (TE)).

In the ternary eutectic composite prepared by FZ, TiC(220), TiB₂(100), and SiC(111) planes were almost perpendicular to the growth direction since significant orientation was identified by XRD.

Figure 2 shows the TEM image of 34TiC-22TiB₂-44SiC (mol%) ternary eutectic composite prepared by FZ at the cross-section perpendicular to the growth direction (a) and the electron diffraction patterns at the interface of TiC-TiB₂ (b) and TiB₂-SiC (c) [3]. The index from TiB₂ spots were painted by yellow in color (Fig. 2 (b) and (c)). The ED patterns of TiC[011] and TiB₂[010] were obtained at the interface of TiC and TiB₂, implying these zone axis were parallel to each other (Fig. 2 (b)). TiC(200) and TiB₂(001) located at the solid line across the (000), suggests that these planes are parallel to each other. TiC(1$\overline{1}$1) and TiB₂(10$\overline{1}$) located at the dash line through the (000), indicates that these planes are also parallel to each other. At the interface of TiB₂ and SiC grains, the relationship of TiB₂[010]// SiC[112], TiB₂(001)//SiC(40$\overline{2}$) and TiB₂(101)//SiC($\overline{2}$20) were obtained. Therefore, the ternary eutectic composite prepared by FZ had the parallel relation of directions and planes: TiC[011]// TiB₂[010]//SiC[112], TiC(200)//TiB₂(001)//SiC(40$\overline{2}$) and TiC(111)// TiB₂(10$\overline{1}$)// SiC($\overline{2}$20).

References

[1] W. J. Li, R. Tu and T. Goto: Mater. Trans. **47**, 1193-1197 (2006).

[2] W. J. Li, R. Tu and T. Goto: Mater. Lett. **60**, 839-843 (2006).

[3] R. Tu, W. J. Li and T. Goto: Mater. Sci. Forum **534-536**, 1057-1060 (2007).

Contact to
Takashi Goto (Multi-functional Materials Science Division)
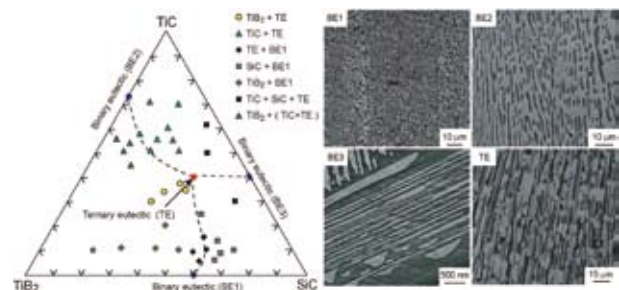e-mail: goto@imr.tohoku.ac.jp

Fig. 1 Phase diagram of TiC-TiB₂-SiC system and microstructure of binary eutectic 40TiB₂-60SiC (BE1), 28TiB₂-72TiC (BE2) and 40TiC-60SiC (BE3) and ternary eutectic 34TiC-22TiB₂-44SiC (mol%) (TE) composites.
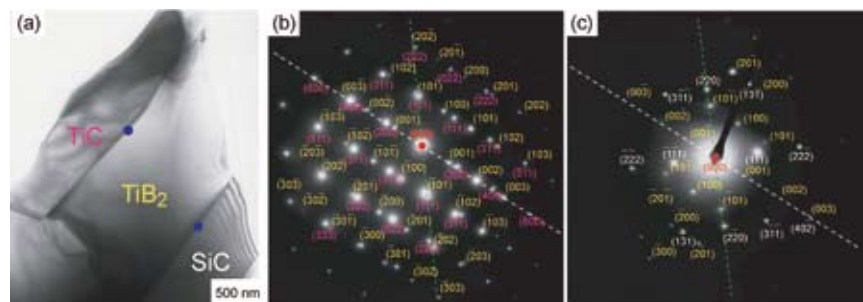

Fig. 2 TEM image of 34TiC-22TiB₂-44SiC (mol%) ternary eutectic composite perpendicular to growth direction (a) and the electron diffraction patterns at the interface of TiC-TiB₂ (b) and TiB₂-SiC (c). (yellow in color: TiB₂)

Ti-Nb-Sn and Ti-V-Sn Alloys with Low Young's Modulus and High Strength

Low Young's modulus at and around 50 GPa is obtained for Ti-Nb-Sn and Ti-V-Sn alloys consisting of martensitic microstructures. Strength increases more than 850 MPa by the thermo mechanical processing utilizing the stress induced and reversed martensitic transformation for Ti-Nb-Sn alloy and the rolling texture development for Ti-V-Sn alloy.

Titanium alloys with low Young's modulus and high strength are strongly demanded in various fields. Many Ti-V base alloys for industrial applications like suspension spring and several Ti-Nb base alloys for biomedical applications have been developed to meet these demands. In this work, microstructures and mechanical properties for Ti-Nb-Sn and Ti-V-Sn alloys were investigated.

In metastable β (Ti-35%Nb)-4%Sn alloy, microstructure undergoes the stress induced martensitic transformation (β/α") with [010]α" cold rolling texture by cold rolling, and evolves into the refined β microstructure with grain size less than 1μm after reversion from stress induced α" to β by 523 K heat treatment [1]. Figure 1 demonstrates the (a) Young's modulus, (b) ultimate tensile strength and (c) elongation to fracture in (Ti-35mass%Nb)-4mass%Sn alloy at various processing conditions. In Fig. 1(a), constituent phases identified by XRD and TEM are also shown. As compared with the Young's modulus of quenched (Ti-35%Nb)-4%Sn alloy, Young's modulus decreases by cold rolling and recovers to the initial value by heat treatment at 523 K for 7.2 ks. The decrease of Young's modulus will be ascribed to the α" formation with (200)α"[010]α" texture, while the recovery of Young's modulus to the value of quenched sample by heat treatment at 523 K for 7.2 ks will be related to the reversion to β phase. On the other hand, marked increase in Young's modulus with increasing the holding time to 93.6 ks of 523 K heat treatment can be seen. Then, it would be ascribed to the α precipitation and its increase in volume fraction. As shown in Fig. 1(b) and (c), by cold rolling and the subsequent heat treatment at 523 K strength increases, while elongation decreases. After cold rolling and the subsequent heat treatment, refined β structure and α precipitates are formed. Therefore, the increase in strength after this thermo-mechanical processing is reasonably explained by this microstructural evolution.

In martensite α' Ti-V-Sn alloy, Young's modulus shows the value from 52 to 60 GPa by optimizing the composition [2]. Therefore, it is suggested that a new type α' martensite Ti-V-Sn alloy with low Young's modulus is expected to substitute for metastable β Ti-V base alloy. Furthermore, cold rolling is effective for decreasing Young's modulus in rolling direction due to the texture formation that rolling direction is parallel to the orientations in basal plane of h.c.p. structure. Figure 2 shows the stress-strain curves of quenched and cold rolled α' martensite (Ti-8%V)-4%Sn alloy. Strength drastically increases by cold rolling, and shows the ultimate tensile strength higher than 1000 MPa, while elongation does not so decrease by cold rolling. After cold rolling, microstructure of acicular α' structure for quenched condition evolves into refined cell like dislocation structure. So the drastic increase in strength after cold rolling as shown in Fig. 2 should be concluded to be due to the refined α' structure.

Thus, it is found that low Young's modulus and high strength can be obtained in Ti-Nb-Sn alloys by utilizing martensitic transformation and in Ti-V-Sn alloys by rolling texture formation.

References
[1] H. Matsumoto et al., J.Alloys and Comp, **439**, 146 (2007).
[2] H. Matsumoto et al., Metall. Trans. **37A** , 3239 (2006).

Contact to
Hiroaki Matsumoto (Deformation Processing Division)
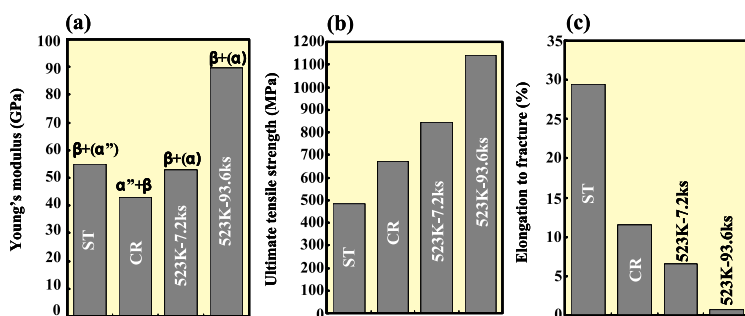e-mail: matumoto@imr.tohoku.ac.jp

Fig. 1 (a) Young's modulus, (b) ultimate tensile strength and (c) elongation to fracture in (Ti-35mass%Nb)-4mass%Sn alloy at various processing conditions.
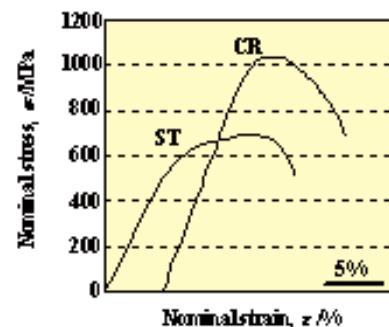

Fig. 2 Nominal stress-nominal strain curves of α' martensite (Ti-8mass%V)-4mass%Sn alloy quenched and cold rolled.

State of Two-dimensional Long-period Superstructure in the Metastable Fe-Nd-B Phase

A new two-dimensional long-period superstructure (LPS) has been discovered in the Fe-Nd-B alloy system, and examined by transmission electron microscopy. The LPS appeared during the crystallization of an Fe-Nd-B amorphous ribbon, and is based on the metastable $D0_3$ phase. This is the first account where LPS with $D0_3$ has ever been reported.

LPS in binary alloys have been known for decades, and in the past, IMR contributed significantly to the understanding of the formation of LPS. For example, the electron diffraction pattern of the CuAu-II phase, in which the tetragonal CuAu-I unit cell with $L1_0$ (Strukturbericht notation) structure shifts by $c/2$ at every M tetragonal cells thus forming a one-dimensional (1D) LPS, was reported as early as 1953. Two-dimensional (2D) LPSs have also been known including the Cu-Pd system. These reported LPS's exist as thermodynamically stable phases, and an approach toward the equilibrium state can experimentally be followed by an appropriate annealing.

Recently, we have discovered 2D LPS in a metastable crystalline phase, which appeared during the first crystallization of Fe-Nd-B amorphous ribbon. This newly found LPS is distinguished from the previously known LPS's in several aspect. First, unlike the LPS's reported so far, the present phase is metastable, and it emerges as an transient phase. Secondly, the LPS is based on the $D0_3$ structure., and include two possible displacement vectors to form the 2D ordered structure. Thirdly, the LPS appeared during the research and development effort in pursuit of so-called spring magnets based on the Fe-Nd-B alloy systems.

Figure 1 shows a schematic model of the two kinds of anti-phase boundaries (APB's) with two types of the displacement vectors, that is possible in the D03 structure, having the composition of AB_3. Here, closed circles denote the A atoms, corresponding to Fe in the present case; open circles the B atoms, corresponding to Nd atoms.

Figure 2 (a) is a selected area diffraction pattern of a spherulite whose [1$\bar{1}$0] zone axis is parallel to the incident electron beam. (Rings arise from the matrix TbCu7-type phase) It can be seen that *hkl* spots with $l=4n\pm2$, *e.g.* 002, split in the [001] direction, while those with $l=4n\pm1$, *e.g.* 111, show an asymmetric two-fold splitting in the [001] and [110] directions. Also notice that these superlattice spots are accompanied with non-negligible diffuse scattering intensity. These splittings indicate the presence of LPS, and can be explained by assuming a 2D LPS, where APBs exist perpendicular to the [001] and [110] directions, with displacement vectors of $1/4a_0$[111] and $1/2a_0$[001], respectively. Figure 2 (b) is a bright-field (BF) image of the spherulite; while Figs.2 (c), (d), and (e) are corresponding dark-field (DF) images taken with 004, 002, and 111 spots, respectively. As can be seen here, the spherulite embedded in the matrix exhibits overall rectangular shape of about 300nm. The DF image taken with the fundamental 004 spot (Fig.2(c)) displays bright contrasts arising from
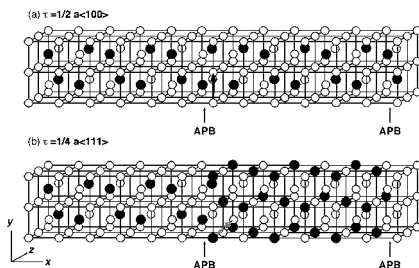
tiny grains from all over inside the spherulite, whereas DF images taken with the superlattice 002 (Fig.2(d)) and 111 (Fig.2(e)) spots show unusual morphology: bright contrasts arise from small grains in the 'core' region of the spherulite, as well as from grains distributed radially towards 'outskirts' of the spherulite. Note also that the bright regions of the spherulite taken with the 002 spot are essentially identical to these taken with the 111 spot, suggesting that these superlattice spots, which exhibit aforementioned different splittings, in fact arise from the same regions of the spherulite.

These observations indicate that the 2D LPS emerged in the following reaction sequence: amorphous -> A2 -> $D0_3$ with 2D LPS -> $D0_3$, where all the phases are metastable. Also, the 2D LPS here can be characterized by $1/4a_0$<111> APBs perpendicular to <100> directions and $1/2a_0$<100> APBs perpendicular to <110> directions, where a_0 is the unit cell parameter of the $D0_3$ cell, with average superperiods of 3.2 and 2.4 nm, respectively.

References
[1] T.J. Konno, M. Uehara, S. Hirosawa, K. Sumiyama and K. Suzuki, J. Alloys Compds. **268**, 278 (1998).
[2] T.J. Konno, M. Uehara, S. Hirosawa, K. Sumiyama and K. Suzuki, Phil. Mag. **A 79**, 2413 (1999).
[2] T.J. Konno, M. Uehara, and S. Hirosawa, Phil. Mag. **86**, 1427 (2006).

Contact to
Toyohiko Konno (Advanced Analysis of Materials Division)
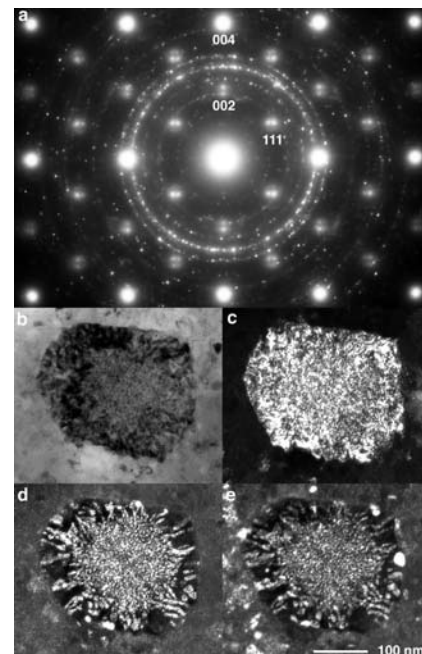e-mail: tjkonno@imr.tohoku.ac.jp

Fig.2 Diffraction pattern and images of a spherulite observed along the [1$\bar{1}$0] zone axis. (a) SAD pattern, showing twofold split of superlattice spots, (b) BF, (c) DF(004), (d) DF(002), and (e) DF(111) images. Note that the spherulite is composed of tiny grains of 2-3 nm, which possess essentially the same cubic orientation, yet (d) and (e) show that ordering to the $D0_3$ phase is incomplete in the outer region of this spherulite.

Fig.1 Schematic models of APBs based on fundamental D03 cells, characterized by two different displacement vectors, τ: (a) $1/4a_0$<111>, (b) $1/2a_0$<100>

LEEM Study of Single-nucleus Polycrystallization in Thin Film Epitaxial Growth

We have observed, by use of low energy electron microscopy (LEEM), the first direct evidence of self-driven polycrystallization evolved from a single nucleus in epitaxial growth of pentacene on the H-Si(111) surface. This finding gives new insight into the crystallization of complex molecular systems, elucidating the importance of nano-scale control of the growth conditions.

The thin film growth of molecular materials is being studied intensely in light of their potential electronic and optical applications. Growth optimization is desired to improve the performance of organic devices. Therefore, it is important to account for the limitations put on the crystal structure, which originate from the intrinsic properties of the material and the growth conditions, and may critically affect the growth mechanism.

Among organic semiconductors, pentacene ($C_{22}H_{14}$) is one of the most widely studied, since it has been successfully employed in organic thin-film transistors. Upon the deposition of pentacene on H-Si(111), LEEM images show single-monolayer high Pn islands with fractal shapes, typical of the DLA-like growth.

Surprisingly, a quite complicated pattern of different contrasts levels is observed in the individual branches of the Pn islands (Fig.1(a)) when the incident electron beam direction is tuned by tilting slightly away from the surface normal in the LEEM experiment. The LEED pattern obtained from the island in Fig.1(a) is shown in Fig.1(b). There are several distinctive features in this pattern. Firstly, the diffraction spots originating form the bare H-Si(111)-1x1 surface are still visible (marked by yellow circles in Fig.1(b)), showing that nucleation of the Pn islands starts immediately without formation of a wetting layer. Secondly, careful analysis of the LEED pattern shows six pairs of double spots, corresponding to six different rotational Pn domains grown epitaxially on the H-Si(111)-1x1 surface.

The above observation makes immediately clear that the different contrast levels in Fig.1(a) originate from different rotational Pn domains, and demonstrates a polycrystalline structure within the single Pn grain, which was observed to develop from a single nucleus [1].
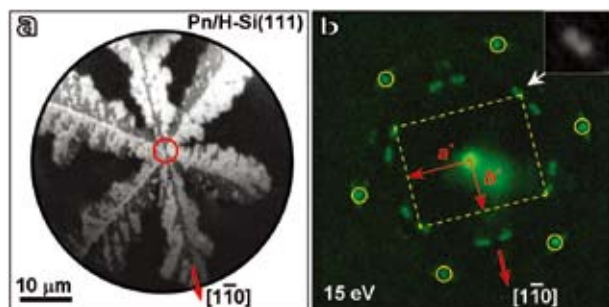
It is found that each individual contrast level can be assigned to one of three micro-beam LEED patterns, corresponding to the Pn *b*-axis (longer in-plane axis) aligning almost exactly (rotated by an angle of 2.3 ± 0.3°) to each of three equivalent <110> directions of the Si substrate surface (Fig.2(a)).

The growth and evolution of the Pn islands into multiple domains are governed by a well-defined set of rules: (1) Branch growth begins with the development of the "main" (center) domain, whose *b*-axis aligns to the one of the <110> directions of the substrate; (2) "Outer" domains grow at each side of the "main" domain with their *b*-axis rotated by ±60°; (3) New ("side") branches grow from the side walls of the "outer" domains replicating procedures (1) and (2), as shown in the Fig.2(b). Even if domains with different orientations are created in random secondary nucleation events, such domains are suppressed by the favored domain (with proper *b*-axis alignment), developing a well defined, polycrystalline structure. Under kinetics-dominated conditions with a significant dendritic growth mode, the formation of side domains whose *b*-axis aligns to the density gradient and develops into a new branch, is preferred over the continuous growth of the center domain.

In conclusion, we have for the first time documented the self-driven polycrystallization in an anisotropic growth system. The observed polycrystallization is a result of kinetic growth processes in conjunction with the intrinsic anisotropy of the crystal (in crystal structure or bonding energy). The observed mechanism can be applied to various systems, in particular, crystallization of organic films, where both kinetic growth conditions and anisotropic effect are present.
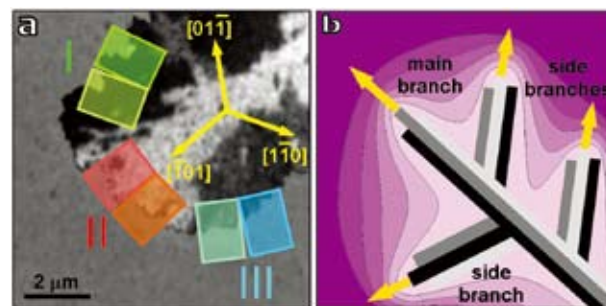

Fig.2. (a) Schematic of Pn 2D crystal alignment reflecting the contrast difference in the polycrystalline domain structure; longer side of each rectangle corresponds to *b*-axis of the 2D unit cell in a particular domain; (b) Sketch illustrating the branching mechanism; the equipotential lines of the density gradient of diffusing molecules are shown schematically (arrows indicate the fast growth directions of the branches, which align to the density gradient).

References
[1] J. T. Sadowski, G. Sazaki, S. Nishikata, A. Al-Mahboob, Y. Fujikawa, K. Nakajima, R. M. Tromp, and T. Sakurai, Phys. Rev. Lett. **98**, 046104 (2007).

Contact to
Jerzy T. Sadowski (Materials Processing and Characterization Division)
e-mail: sadows-0@imr.tohoku.ac.jp

Fig.1. (a) Tilted-beam LEEM image of the pentacene island grown on the H-Si(111) surface (imaging electron energy of 2.2 eV) – at these imaging conditions a complicated domain pattern is visible within the island; (b) LEED diffraction pattern obtained from the island shown in (a); spots originating from Si(111)-1x1 lattice are marked by yellow circles and a unit cell of one of the Pn rotational domains is outlined by a rectangle; magnified image of the pair of spots defining the "paired" Pn domains, rotated with respect to each other by an angle of 4.6 ± 0.3°, is shown in the inset.

Surface Properties of Bulk Metallic Glass: $Zr_{50}Cu_{40}Al_{10}$

Atomic force microscope (AFM) makes it possible to image the morphological evolution of the $Zr_{50}Cu_{40}Al_{10}$ metallic glass surface. The visualizations of ~200 nm nanoclusters and viscous flow like surface features involving crystalline phases are succeeded. The results of Auger electron spectroscopy (AES) confirm that the observed nanoclusters correspond to ZrO surface products. Further, the nanocluster formation does not influence to a crystallization process but the viscous flow is crucial for the surface modification. The temperature dependent observations using AFM combined chemical analysis can be a new protocol to study fundamental properties of metallic glass surfaces [1].

The materials of bulk metallic glass (BMG) have received much attention because they offer extraordinary mechanical properties that have been applied for industrial products such as sub-micro sized gears and liner actuators [2]. There have been developing to pattern and fabricate features not only for micro-electro mechanical system but also for much smaller sized fabrications toward nano-electro mechanical system. Most studies of BMG have focused on both growth development of ingot sizes and improvement for multi mechanical properties including static and dynamic mechanical strength, toughness, and fatigue. However, far less attention paid for surface properties of BMG though they play an important role for nano- sized components where surface effects cannot be ignored.

Here we demonstrate surface morphological evolutions induced by thermal heating from the amorphous solid into the supercooled liquid region. Figure 1(a) shows the surface morphology after the heating at 673 K. Scratches run diagonally across the image and the width is about few hundreds nm. They were created during mechanical polishing. The average surface roughness that is defined by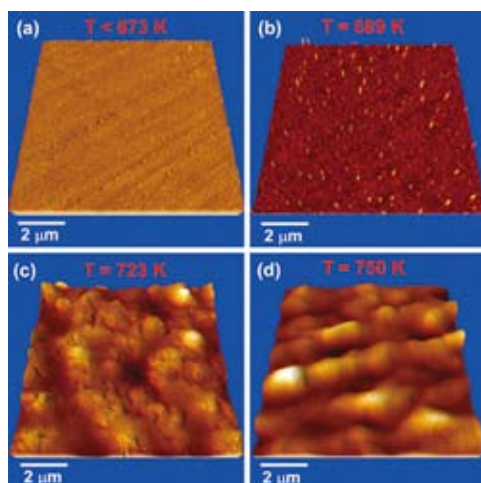 the absolute value of surface heights averaged over the scanned area of 10 x 10 μm^2 is 12 nm. Figure 1(b) shows the surface morphology at 698 K. Surprisingly, there are nano-sized structures created by thermal heating in the vacuum below 1 x 10^{-8} Torr. The image of Fig. 1(c) demonstrates very different morphology where the nanostructures disappeared but viscous flow like features appeared at 723 K. Height analysis shows that the maximum vertical interval between features is ~30 nm in this image. The crystallization was confirmed by ex-situ X-ray diffraction at this temperature. When the sample was heated at 748 K, viscous features drastically enhanced having chain of large mountains, as shown in Fig. 1(d). The maximum height interval between mountains is ~150 nm and mountains are separated about 3-4 μm.

To obtain the relationship between the morphological changes and the surface compositions, we carried out AES. The AES results reveal that the nanoclusters are composed from residual ZrO surface products because of the existence of surface oxygen even at 748 K. At this temperature, the intensity of O remains in double ration compared with that of Zr, indicating the formation of a ZrO_2 layer. Above the glass transition temperature (~700K), the nanoclusters are disappeared while the crystallization is confirmed. Thus, these nano-products do not affect the crystallization process.
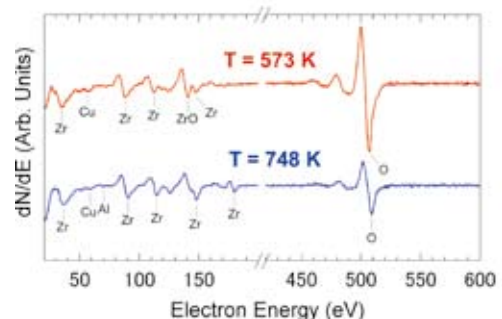

Fig. 2 AES spectra were measured at 573 and 748 K under the vacuum of ~10^{-9} Torr. At 573 K, 36 eV: Zr NVV, 59 eV: Cu MVV, 91 and 115 eV: Zr MNN, 141 eV: ZrO chemical shift, 147 eV: Zr MNN, and 509 eV: O KLL transition peaks were identified. At 748K, in addition to the results at 573K, 69 eV: Al LVV, 180 eV: Zr MNN transition peaks were obtained.

References
[1] K.S. Nakayama, Y. Yokoyama, T. Sakurai, and A. Inoue, Appl. Phys. Lett. **90**, 183105 (2007).
[2] N. Nishiyama, K. Amiya, and A. Inoue, Mater. Trans. **45**, 1245 (2004).

Contact to
Koji S. Nakayama (Research and Development Project on Advanced Metallic Glasses, Inorganic Materials and Joining Technology)
e-mail: kojisn@imr.tohoku.ac.jp

Fig. 1 AFM images were obtained after the heating at (a) 673 K, (b) 698 K, (c) 723 K, and (d) 748 K in the vacuum below 1x10^{-8} Torr. Above 723K, the crystallization phases were confirmed by XRD.

Electronic Rule for Formation of Glassy Alloys

The glass transition temperature T_g of 100 kinds of glassy alloys can be expressed as a function of their valence electron concentration (VEC): T_g = 131VEC +57 for metal/metal bonding type and T_g = -236VEC +2375 for metal/metalloid bonding one. The resonance bonding of the glassy alloys could be caused by spd or spf hybridization.

The concept of "valence electron" has been derived by Pauling for elements as they are bonded in the crystalline metallic state. The valence electrons are defined as outer freely-moving s and p or d electrons that are not bound to any particular cations. On the other hand, the distinguishing feature of glassy alloys without crystal structure is the randomness of their potential energy. The potential energy minimum among atoms in the multi-component metallic glass is not as rigid as that of crystal alloys, so that the wave functions of these electrons are irregularly spread out much more in space than those of the crystalline metallic valence electrons.

Our interest lies in studying thermal stability of glassy alloys as the function of their valence electron concentration in terms of amorphous metallic bonding, using 100 kinds of the glassy alloys. The VEC in the glassy alloys (II_A, III_B, IV_C, V_D, VI_E, VII_F, $VIII_G$) and (II_A, III_B, IV_C, V_D, VI_E, VII_F, $VIII_G$) ($M_x)_w$ (M= B, C, Si, P, Ge, Sn, Sb, Bi) respectively, of group II to VIII elements has been defined as follows:[2, 3]

$$VEC = II_A + III_B + IV_C + V_D + VI_E + VII_F + VIII_G$$
for metal/metal type, (1)

$$VEC = II_A + III_B + IV_C + V_D + VI_E + VII_F + VIII_G + \Sigma M_i X_W$$
for metal/metalloid type, (2)

where A, B, C, D, E, F and G are atomic fractions, A+B+C+D+E+F+G =1 and$\Sigma M_i X$=1. The VEC for 83 kinds of ternary and 17 kinds of quaternary Pd-, Zr-, Fe-, Ni-, Co-, Cu-, Mg-, Ti-, Hf-, Au-, Pt-, La- and Be- based glassy alloys have been calculated using electron valences of 35 kinds of their constituent elements. After we assigned the electron valence from 1 to 15 for s, p, d and f orbits in all elements, taking multiple orbital electron hybridization into consideration, based on the standard method of least squares, we repeatedly calculated up till we can obtain the best linearity for the correlation between T_g and VEC. The best result is shown in Fig.1, for metal/metal and metal/metalloid bonding types. Both type alloy groups show fairly good linearity, r =0.913 and 0.906, respectively. To certificate application of VEC for the electronic rule, we calculated the stability for anionic clusters by an excess amount of electrons transferring from inner orbital d or f electrons, in comparison with the stability for neutral one. We can conclude that the increase in the valence of magnesium stabilizes the cluster structures and affirms positively the application of VEC for the electronic rule associated with the stability of glassy alloys. Thus, the stable region for formation of the glassy phase would be 2.6 < VEC < 5.3 and 6.7 < VEC < 8.8 for metallic- and metalloid- type metallic glasses, respectively. This means that transition metal elements with higher valence (e.g. group VIII and Ib elements) are the most desirable ones for the formation of glassy alloys with higher T_g. The resonance bonding of the glassy alloys could be caused by spd or spf hybridization. As corroborating evidence, X-ray photoelectron spectroscopy analysis of glassy alloy Zr55Al10Cu30Ni5 suggested that stabilization in the glass phase is derived from formation of a pseudo gap below Fermi energy E_F due to spd hybridization.
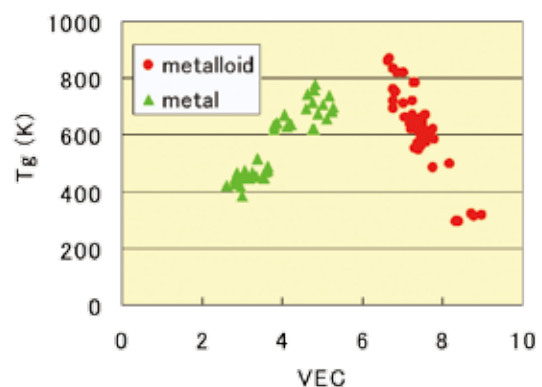

Fig. 1 Relation between T_g and VEC for 100 kinds of glassy allows: green and red solids are metal/metal and metal/metalloid bonding types, respectively.

References
[1] M.Fukuhara, M.Takahashi, Y.Kawazoe and A.Inoue, Appl.Phys.Lett. **90**, 073114 (2007).
[2] M.Fukuhara, T.Mitsuda, Y.Katsumura and A.Fukawa, J.Mater.Sci. **20**, 710 (1985).
[3] M.Fukuhara and H. A.McKinstry, Phys.Stat.Sol.(b) **157**, 357 (1990).

Contact to
Mikio Fukuhara (Research and Development Project on Advanced Metallic Glasses, Inorganic Materials and Joining Technology)
e-mail: fukuhara@imr.tohoku.ac.jp

Period icity	2 (IIa)	3 (IIIa)	4 (IVa)	5 (Va)	6 (VIa)	7 (VIIa)	8 (VIII)	9 (VIII)	10 (VIII)	11 (Ib)	12 (IIb)	13 (IIIb)	14 (IVb)	15 (Vb)
2	Be 2.4											B 3.0	C 4.0	
3	Mg 2.4											Al 3.0	Si 4.0	P 5.0
4		Y 3.0	Ti 4.0	V 5.0	Cr 6.0	Mn 6.0	Fe 6.1	Co 6.1	Ni 6.2	Cu 5.8			Ge 4.0	
5		La, Ce, Nd 3.0	Zr 4.5	Nb 5.4	Mo 6.1			Rh 6.2	Pd 6.5	Ag 6.0			Sn 4.0	Sb 5.0
6			Hf 4.6	Ta 5.5	W 6.3			Pt 6.6		Au 7.2			Pb 4.0	Bi 5.0

Table 1 The electron valence for elements used in this study. Light yellow, light green, light pink and light blue present s-, p-, d- and f- electrons.

Evolution of Size Enlargement of Bulk Metallic Glasses

In order to try enlargement of Zr-based bulk glassy alloy, the purity of the master alloy was enhanced and supercool solidification was also analyzed. As a result, the sort of crystal phase changes to simple structure by purity enhancement. Therefore, high-purified metallic glass forming master alloy makes more than 300K supercooling possible easily. Furthermore, in casting, the cap-cast method in which three-dimensional cooling is possible was developed, and it succeeded in enlargement of bulk metallic glasses up to ϕ30mm.

The solidification morphology and structure of arc-melted $Zr_{50}Cu_{40}Al_{10}$ glass-forming alloys were examined [1] to determine the impurity influences using two grades of Zr metals: "sponge Zr" purified somewhat but not highly by the Kroll method, and highly purified "crystal Zr". When crystal Zr is used, arc-melted $Zr_{50}Cu_{40}Al_{10}$ alloy exhibits superior glass-forming ability in forming glassy phase, even in a 40g weight master alloy. When sponge Zr is used, we can see distinct a chain reaction of exothermic heat due to crystallization after vitrification during solidification. Therefore, we can obtain metallic shinning master alloy meaning complete vitrification in the topside of master alloy as shown in Fig. 1 (a). Furthermore, vitrification in front of the solidification interface of arc-melted $Zr_{50}Cu_{40}Al_{10}$ alloy with crystal Zr can occur when the growing crystalline phase is an Al-supersaturated B2 (B19') -type ZrCu phase.
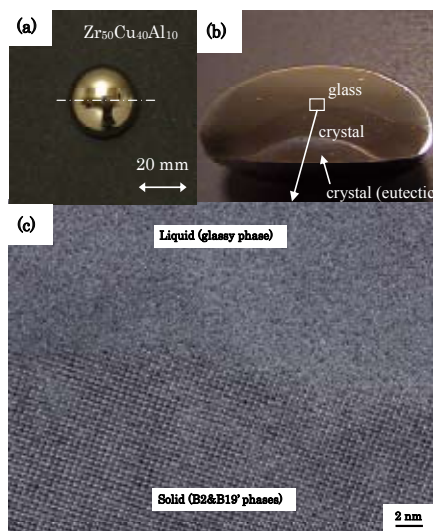

Fig. 1 Outer view (a), cross sectional optical micrograph image (b) and high-resolution transmission electron micrograph image of the interface between the glassy and crystalline phases (c) of arc-melted high-purified $Zr_{50}Cu_{40}Al_{10}$ ingot.

A HRTEM image of the crystal/glass interface of supercooled solidified high-purity $Zr_{50}Cu_{40}Al_{10}$ alloy is shown in Fig. 1 (c). No nanocrystalline inclusions were seen in front of the solidified interface, moreover, the solid/liquid interface is flat. Both of these morphologies suggest that the temperature gradient at the crystal/glass interface was not very steep. Careful observation of the HRTEM image shows "onion-like" contrast [2], which suggests the existence of a cluster in liquid in front of the crystallized interface. Additionally, a little Zr-diluted and Cu-enriched compositional fluctuation, whose absolute values were less than a few at%,

was observed at the crystal→glass interface by nanobeam EDS. No change in the Al concentration was observed around the interface, however, a significant fluctuation in the Al concentration in the early stage of eutectic regions as shown in Fig. 1 (b). Only the high purified master alloy exhibit glassy region with high reliability meaning a superior glass-forming ability.

By use of high-purified master alloys, we tried enragement of "Inoue's alloy" $Zr_{55}Cu_{30}Ni_5Al_{10}$ with modified tilt-cast method [3] called cap-casting method. As shown in Fig. 2 (a), we succeeded in producing a larger sized glassy alloy rod of 30 mm in diameter by the cap cast technique. Fig. 2 (b) shows the absence of crystalline inclusion over the cross sectional area at the site of 10 mm from the bottom side. The X-ray diffraction pattern of the cross section shown in Fig. 2 (c) is also composed of distinct Bragg peaks, implying the formation of a single glassy phase.
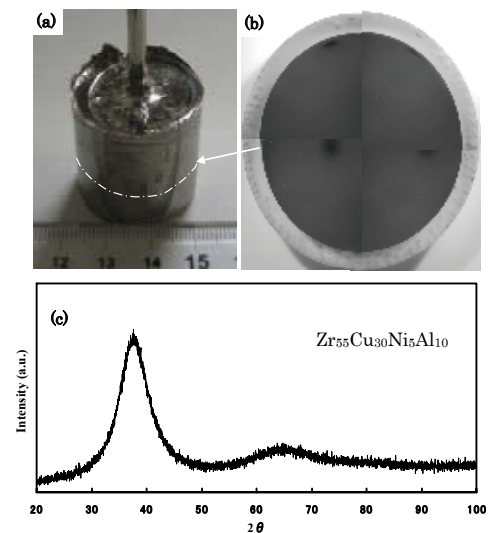

Fig. 2 Outer appearance of (a) cast rod, (b) cross sectional image at dot line and (c) X-ray diffraction pattern of the $Zr_{55}Cu_{30}Ni_5Al_{10}$ glassy rod (ϕ30mm) prepared by the cap-cast method.

With the aim of producing a much larger sized bulk glassy alloy, a cap-cast technique, leading to achieve a higher cooling rate even in an upper region, was developed by modification of the tilt casting technique. We succeeded in the production of a glassy $Zr_{55}Cu_{30}Ni_5Al_{10}$ alloy rod with a diameter of 30 mm.

References
[1] Y. Yokoyama, H. Fredriksson, H. Yasuda, M. Nishijima and A. Inoue, Materials Transactions, **48**, No6 1363 (2007).
[2] J. Saida, M. Matsushita and A. Inoue: Appl. Phys. Lett., **79**, 412 (2001).
[3] Y. Yokoyama, K. Inoue and K. Fukaura, Mater. Trans. **43**, 2316 (2002).

Contact to
Yoshihiko Yokoyama (Advanced Research Center of Metallic Glasses)
e-mail: yy@imr.tohoku.ac.jp

Nano-sized Deformation and Failure of Ultrahigh Strength Materials

Ultrahigh strength materials, such as bulk metallic glasses, nanocrystalline metals and high performance ceramics, can withstand very high stresses prior to failure. Nevertheless, the underlying micro-mechanisms that control the deformation and damage remain to be comprehensively clarified. Our recent investigations reveal that the mechanical behaviour of these ultrahigh strength materials is associated with localized shearing and deformation-induced phase transitions.

The superior mechanical properties of bulk metallic glasses, nanocrystalline metals and high performance ceramics, such as ultrahigh strength and extraordinary elasticity have made them ideal candidates in micro-/submicro-scale applications, e.g., MEMS and NEMS, where both high strength and small part sizes are required. Thus, the efforts to characterize their deformation and damage mechanisms are important for modeling their performances and developing new materials with improved properties. In recent years, we employed transmission electron microscopy and Raman spectroscopy to investigate plasticity and failure of the ultrahigh strength materials. Our preliminary results suggest that nonlinear deformation of these high strength materials is associated with localized deformation and phase transitions, mainly within nano-sized shear bands.

Figure 1 shows a narrow shear band in shock-loaded boron carbide, one of the hardest materials. The plastic deformation of this material takes place at high pressures and is mainly carried by the 2-3 nm wide shear bands [1]. The operation of the local shearing was found to accomplish by a phase transition that the crystalline phase turns to be amorphous within the narrow shear bands. The amorphization induced lattice changes can provide irreversible plastic strains. Meanwhile, the amorphous bands with low strength cause the catastrophic failure of the high strength materials. This stress-induced amorphization has been observed in a number of other hard materials, such as silicon and boron nitride. However, with certain loading conditions, the high strength ceramics sometimes exhibit metal-like plasticity. An example is high purity alumina subjected to plate impacts. Well-defined dynamic yielding can be observed, which is proved to be performed by global twinning. These twinning planes act as the preferred paths for subsequent cleavage and lead to materials failure [2].

Different from the high-strength inorganic materials in which stress-induced localized phase transitions lead to material failure, we found that deformation induced microstructural evolution in high strength metallic materials, such as bulk metallic glasses and nanocrystalline metals, benefits the ductility. More recently, extraordinary plasticity and work hardening were observed in Cu- and Pt-based monolithic BMGs with high strength. Although a number of explanations have been suggested, including high Poisson's ratio and structure inhomogeneity, the underlying physical mechanism, in particular microscopic explanation, remains mystery. We employed high-resolution electron microscopy to characterize the atomic structure of shear bands in these ductile BMGs. Our observations reveal a novel self-locked effect in ductile bulk metallic glasses. Strain softening caused by localized shearing can be effectively prevented by the crystalline nanoparticles that are in situ produced by plastic flow within the shear bands (Fig. 2), leading to large plasticity and strain hardening. These atomic-scale observations not only well explain the extraordinary plasticity that was recently observed in the materials, but also reveal a novel deformation mechanism that can effectively improve the ductility of monolithic metallic glasses.

Understanding the micromechanisms of the deformation and failure of untrahigh strength materials is an interesting topic for both basic and applied research. The well-defined physical mechanisms will allow for more robust models to predict the their mechanical performances and lead the way toward processing improved materials.
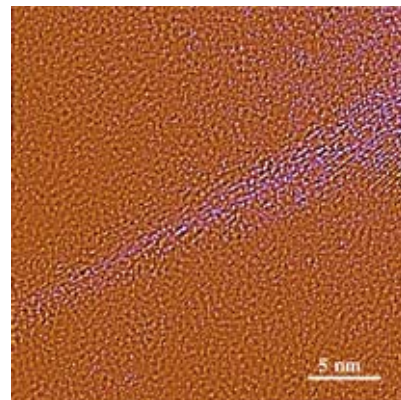
Fig. 2 Self-locked shear bands in a ductile $Zr_{50}Cu_{50}$ BMG with deformation-induced nanocrystallie particles

References
[1] M. W. Chen, J. W. McCauley and K. J. Hemker, Science **299**, 1563 (2003).
[2] M. W. Chen, J. W. McCauley, D. Dandekar and Bourne, Nature Materials **5**, 614 (2006).
[3] M. W. Chen, A. Inoue, W. Zhang and T. Sakurai, Phys. Rev. Lett. **96**, 245502 (2006).

Contact to
Mingwei Chen (International Frontier Center for Advanced Materials)
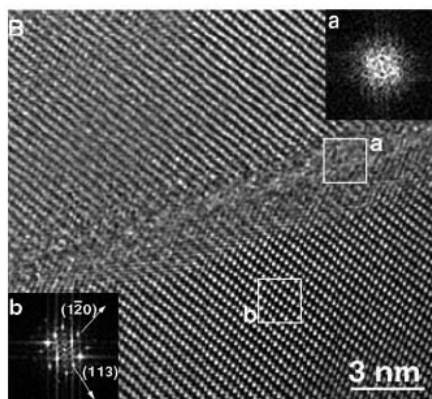e-mail: mwchen@imr.tohoku.ac.jp

Fig. 1 Nano-sized shear band in shock-loaded boron carbide. The high resolution transmission electron microscopy reveals that amorphization takes place within the 2-3 nm wide bands.